Can We Enhance Passivity with a Surface Finish? Spectroscopic and Electrochemical Analysis on 316L Stainless Steel

Shova Neupane, Sandrine Zanna, Antoine Seyeux, Lorena H Klein, Vincent Maurice, Philippe Marcus

Journal of The Electrochemical Society

OPEN ACCESS

Can We Enhance Passivity with a Surface Finish? Spectroscopic and Electrochemical Analysis on 316L Stainless Steel

To cite this article: Shova Neupane *et al* 2022 *J. Electrochem. Soc.* **169** 011505

Journal of The Electrochemical Society, 2022 **169** 011505

Can We Enhance Passivity with a Surface Finish? Spectroscopic and Electrochemical Analysis on 316L Stainless Steel

Shova Neupane, Sandrine Zanna, Antoine Seyeux, Lorena H. Klein, Vincent Maurice,[z] and Philippe Marcus[*,z]

PSL Research University, CNRS - Chimie ParisTech, Institut de Recherche de Chimie Paris (IRCP), Physical Chemistry of Surfaces Group, 11 rue Pierre et Marie Curie, 75005 Paris, France

The effects of surface finish by mechanical polishing, vibratory polishing, and high-temperature annealing were studied on 316L stainless steel by combining microscopic and spectroscopic analysis of the surface morphology and composition and electrochemical analysis of the corrosion resistance. Compared to mechanical polishing, vibratory finishing promotes passivity at the active-passive transition in acid solution and enhances resistance to chloride-induced passivity breakdown. Cr and Mo enrichments in the native oxide film increase owing to preferential iron etching. The bilayer structure develops a thicker Cr(III) oxide inner barrier layer and an outer exchange layer further enriched in Cr(III) hydroxide and Mo(IV/VI) oxides. The Fe-rich weak sites of passivity are reinforced. High-temperature annealing in reducing hydrogen environment enables us to fully reconstruct the cold-worked layers left by mechanical or vibratory finishing, thus allowing us to expose the bulk microstructure at the topmost surface. The benefits brought by vibratory finishing are lost upon reducing the initial native oxide. The re-formed native oxide develops a bilayer structure with similar Cr and Mo enrichments as that obtained from mechanical polishing and no beneficial effects on passivity. The results provide comprehensive insight into how the passivity of stainless steel can be enhanced by surface enrichment engineering.

 [DOI: 10.1149/1945-7111/ac4bf7]

Manuscript submitted November 30, 2021; revised manuscript received January 7, 2022. Published January 27, 2022.

Supplementary material for this article is available online

Stainless steels (SS) are practical and cost-effective options for countless metal parts used in industries as well as in everyday life due to their unique mechanical and corrosion resistance properties. New grades are regularly developed for demanding applications, and research is ongoing to deepen our understanding of the surface properties, including the knowledge of the mechanisms governing the formation and stability of the oxide passive film that provides self-protection against corrosion. The passive film formed in corrosive aqueous media is nanometer thick and enriched in Cr (III) oxide species, which is the key for efficient passivity due to the higher stability of these species compared to Fe(II) and Fe(III) oxide species.[1–9] On most common austenitic grades such as AISI SS304 (Fe-Cr-Ni) and SS316 (Fe-Cr-Ni-Mo), Ni(II) oxide species are found at very low concentrations when detected, and metallic nickel is enriched in the metallic alloy region underneath the oxide layer.[10–16] Molybdenum added at a few percent level in the alloy increases the corrosion resistance in chloride-containing environments. The passive film is enriched in Mo(IV) and Mo(VI) oxide species,[7,11–13,17–20] which has been proposed to increase its resistance to chloride-induced breakdown.[18,21–23] The presence of Mo in the alloy has also been proposed to promote self-repair after passivity breakdown.[10,16,20,24–26] Recent studies have revealed that the Cr(III) enrichment at the surface is not homogenous at the nanometer scale as a result of the pre-passivation mechanisms of oxidation by which the native oxide is initially formed,[27–29] and it has been proposed that this nanoscale heterogeneity can trigger local passivity breakdown in corrosive environment followed by initiation of localized corrosion in the absence of self-repair.[30–34]

The native oxide film, obtained after surface preparation and prior to passivation in aggressive environment, has been thoroughly investigated by surface analysis, including by Time-of-Flight Secondary Ion Mass Spectroscopy (ToF-SIMS) and X-ray Photoelectron Spectroscopy (XPS). On SS316L, it has a stratified bilayer structure with Cr(III) oxide concentrated in the inner layer and Cr(III) hydroxide concentrated in the outer layer together with the Fe(II), Fe(III) and Mo(IV), Mo(VI) oxidized species.[22,30–32,35] Cr and Mo, the two key elements for efficient and durable corrosion resistance, are already enriched in the native oxide film and become further enriched after passivation in low pH corrosive media owing to the preferential dissolution of iron oxide species in the acidic solution.[11,24,30–33,36,37] Strategies to increase the enrichment of these two elements in the surface oxide film in the pre-passivation stage prior to exposure to a corrosive media possibly rely on controlling the growth mechanisms of the surface oxide, for instance, by exposing the oxide-free surface to ultra-low pressure gaseous oxygen.[30,31,33] However, more readily applicable surface finish methods for promoting Cr and/or Mo enrichment are also to be studied.[10,37–39]

Mechanical polishing is a commonly applied finishing process for surface preparation in corrosion studies of metals, including SS. It allows homogenizing the surface by minimization or elimination of the major imperfections and dirt. However, there are other surface finishes that can also be applied to further improve the surface quality and remove, at least partially, the cold-worked layer left by mechanical polishing, such as vibratory polishing, annealing at high temperatures, and electropolishing. Vibratory polishing is popular in industries due to the advantages inherent to the method in terms of ease of use, automation, and material handling. The vibratory action creates friction through vibration to rub the sample against grinding particles. A sample can thus be deburred and more smoothly eroded than with classical, non-vibratory mechanical polishing.[40,41] High-temperature annealing promotes long-range surface atomic mobility, which enables relief of the surface stress accumulated in the cold-worked layer and thus reveals the bulk structure by reconstructing the topmost surface.[1,2,14,27,29,42] Electropolishing dissolves the cold-worked layer, thus revealing the underlying microstructure, but the surface does not reconstruct like with high-temperature annealing in reducing atmosphere due to limited atomic transport, and thus exposes a non-equilibrium structure.[41,43–47]

In the present work, we addressed the effects of surface finishing by vibratory polish and high-temperature annealing in reducing atmosphere as compared to classical mechanical polishing on the composition and thickness of the native oxide film obtained on SS316L samples, on the passivation behavior in aqueous acid

*Electrochemical Society Fellow.
[z]E-mail: vincent.maurice@chimieparistech.psl.eu; philippe.marcus@chimieparistech.psl.eu

solution, and the resistance to the initiation of chloride-induced localized corrosion. Surface topology was characterized by Optical Microscopy (OM) and Atomic Force Microscopy (AFM). ToF-SIMS and XPS were applied to characterize the stratified structure, thickness, and composition of the native oxide film. Potentiodynamic polarization was performed to analyze the passivation properties, and potentiostatic polarization was applied to study the resistance to passivity breakdown and the initiation of localized corrosion by pitting. The results provide insight into how the passivity of stainless steel can be enhanced.

Experimental

Low carbon SS316L polycrystalline samples were used. Nominal composition was Fe-18/20Cr-13Ni-2.7Mo (w%) with 0.03% max C, 2% max Mn, 0.75% max Si, 0.040% max P, 0.03% max S and 0.10% max N. All samples were mechanically polished first with emery paper of successive 1200 and 2400 grades and then with diamond suspensions of successive 6, 3, 1, and 0.25 μm grades, then rinsed in successive ultrasonicated baths of acetone, ethanol, and ultra-pure (UP) water (resistivity $>$ 18 MΩ cm) for 5 min each, and finally dried under filtered compressed air, like applied in previous studies.[22,32,48] The samples studied with this surface finish are labeled TP (traditional polish). For vibratory finishing, a Vibrotech300 polisher was used. Vibratory polishing was applied for 5–6 h at a vibration amplitude of 47 μm and frequency of 47 Hz. A diamond suspension of grade 0.25 μm mixed in alcohol-based lubricant at a volume ratio of 1:1 was used. Rinsing and drying procedures were the same as for TP samples. The samples submitted to this surface finish are labeled VP (vibratory polish). The samples labeled TP + HTA and VP + HTA were TP and VP samples, respectively, subsequently treated with high-temperature annealing (HTA). Annealing treatment was performed at 900 °C for ~6 h in a reducing gaseous environment in order to avoid thermal oxidation. After pumping down the annealing chamber containing the samples to a residual pressure of 8–9 $\times$ 10^{-6} mbar at room temperature, hydrogen gas (6 N) was filled in up to atmospheric pressure until a dynamic flow was established. Then, the chamber was heated at the annealing temperature. HT annealing was stopped by quenching the annealing chamber with 0 °C water. The chamber was opened to ambient air to transfer the samples for subsequent analysis.

The electrochemical measurements were performed in a 3-electrode electrochemical cell controlled by a Gamry 600 potentiostat. A Ag/AgCl (saturated KCl) electrode was used as a reference electrode, and a gold coil was used as a counter electrode. The working electrode area was 2.09 cm^2 delimited by a Viton O-ring. Polarization curves were recorded in 0.05 M sulfuric acid (H_2SO_4) prepared from ultrapure chemicals (VWR) and (UP) water. After stabilization for 30 min at open circuit potential (OCP), the potential was scanned linearly (1 mV s^{-1}), starting from a cathodic vertex value negative with respect to OCP and until oxygen evolution. Potentiostatic passivation experiments were performed with the same electrochemical set-up. After 15 min rest at OCP in the chloride-free 0.05 M H_2SO_4 electrolyte, the potential was stepped to 0.3 V_{SHE}, in the middle of the passive domain. After 1 h of passivation in the chloride-free solution, chloride ions were added step-wise every 10 min with 0.1 M increments in concentration until initiation of localized corrosion was observed. The chloride-containing 0.05 M H_2SO_4 additive electrolyte was prepared with sodium chloride (NaCl) crystal (VWR) first dissolved in UP water.

For surface topology analysis, a digital Keyence VHX-500 optical microscope with lens magnification of 100*1000 and 500*5000 and a Nano-observer AFM microscope from CSI instruments were used. The AC oscillatory mode of AFM was used with a silicon probe from AppNano, USA, operating at a resonance frequency of 50–70 kHz and with a cantilever spring constant (k) of 1–5 N m^{-1}. The recorded raw image files were converted to portable images with the Gwyddion (64 bit) software [49] without further processing.

Depth profile elemental analysis was performed with an IONTOF ToF-SIMS 5 spectrometer operating at a base pressure of about 10^{-9} mbar. Data acquisition and post-processing were made by

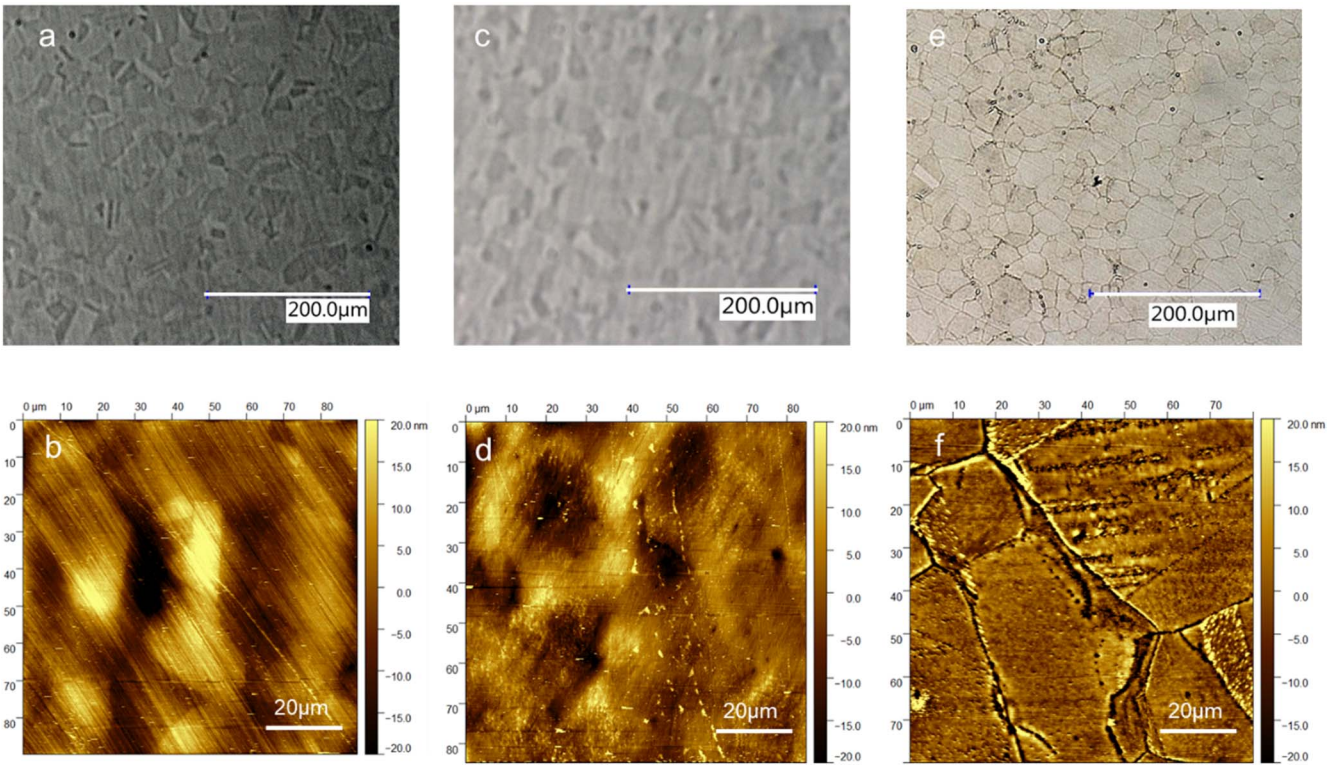

Figure 1. OM and AFM images of (a), (b) traditionally polished (TP), (c), (d) vibratory polished (VP), and (e), (f) traditionally polished and high temperature annealed (TP + HTA) polycrystalline SS316L samples.

using the IONSPEC 6.5 software. The depth profiles were recorded in dual-beam mode. A pulsed 25 KeV Bi + primary ion source delivering 1.2 pA of target current over a 100 × 100 μm^2 area was used for analysis. The Bi^+ primary ion flux was sufficiently low to ensure analysis in static SIMS conditions. Analysis was interlaced with sputtering using a 0.5 keV Cs^+ sputter beam delivering 20 nA of target current over a 300 × 300 μm^2 area. Both ion beams were at the incidence of 45° with respect to sample surface and well-aligned to ensure analysis from the center of the sputtered crater. Negative ions were recorded because of their higher sensitivity to fragments coming from oxide matrices.

Surface composition and oxide film thickness were determined by XPS analysis performed with a Thermo Electron ESCALAB 250 spectrometer (base pressure of 10^{-9} mbar). A monochromatized Al K_α X-ray source ($h\nu = 1486.6$ eV) was used. Survey spectra of the photoelectrons were recorded with a pass energy of 100 eV at 1 eV step size, while high-resolution spectra of the selected core levels were acquired with a pass energy of 20 eV at a step size of 0.1 eV. The take-off angle of the analyzed photoelectrons was 90°. Binding energies (BE) were calibrated by setting the C 1 s signal corresponding to olefinic bonds (–CH2–CH2–) at 285.0 eV. Peak fitting was performed with the Avantage software.[50] For fitting the high-resolution spectra, a set of constraints was applied to background subtraction (adjustable Shirley), BE, full width half maximum (FWHM), and line shape of peak components in order to achieve the most accurate and consistent fit. The high-resolution Mo 3d, Cr 2p3/2, Fe 2p3/2, Ni 2p3/2, O 1 s, and C 1 s core-level spectra were reconstructed with the specific self-consistent fitting parameters based on literature.[51]

Results and Discussion

Surface topology.—Figure 1 presents microscopic surface observations of TP, VP, and TP + HTA samples. On the TP surface observed by optical microscopy (Fig. 1a), the different grains of the polycrystalline microstructure are apparent. One can also notice that the surface appears streaked with lines, better seen at closer inspection. In contrast, on the topmost surface imaged by AFM (Fig. 1b), the polycrystalline microstructure is barely distinguished. The surface is homogeneously terminated by the polishing lines left by the surface finish procedure and corresponding to the streaks observed by OM. These lines are a marker of the presence of the cold-worked layer produced by the surface finish and thus indicate that the surface is under residual mechanical stress. The grains are only locally apparent and systematically covered by the cold-worked layer. The Ra roughness of the surface is ∼1 nm.

After VP finish, the polycrystalline microstructure observed by OM remains apparent but with the polishing lines no longer visible, suggesting at least partial removal of the cold-worked layer (Fig. 1c). Accordingly, AFM imaging (Fig. 1d) no longer shows well-marked polishing lines. However, grains and grain boundaries are not clearly revealed at the topmost surface, suggesting that the surface is still terminated by a cold-work layer. Ra roughness measured in Fig. 1d is ∼1 nm. After high-temperature annealing, TP + HTA and VP +

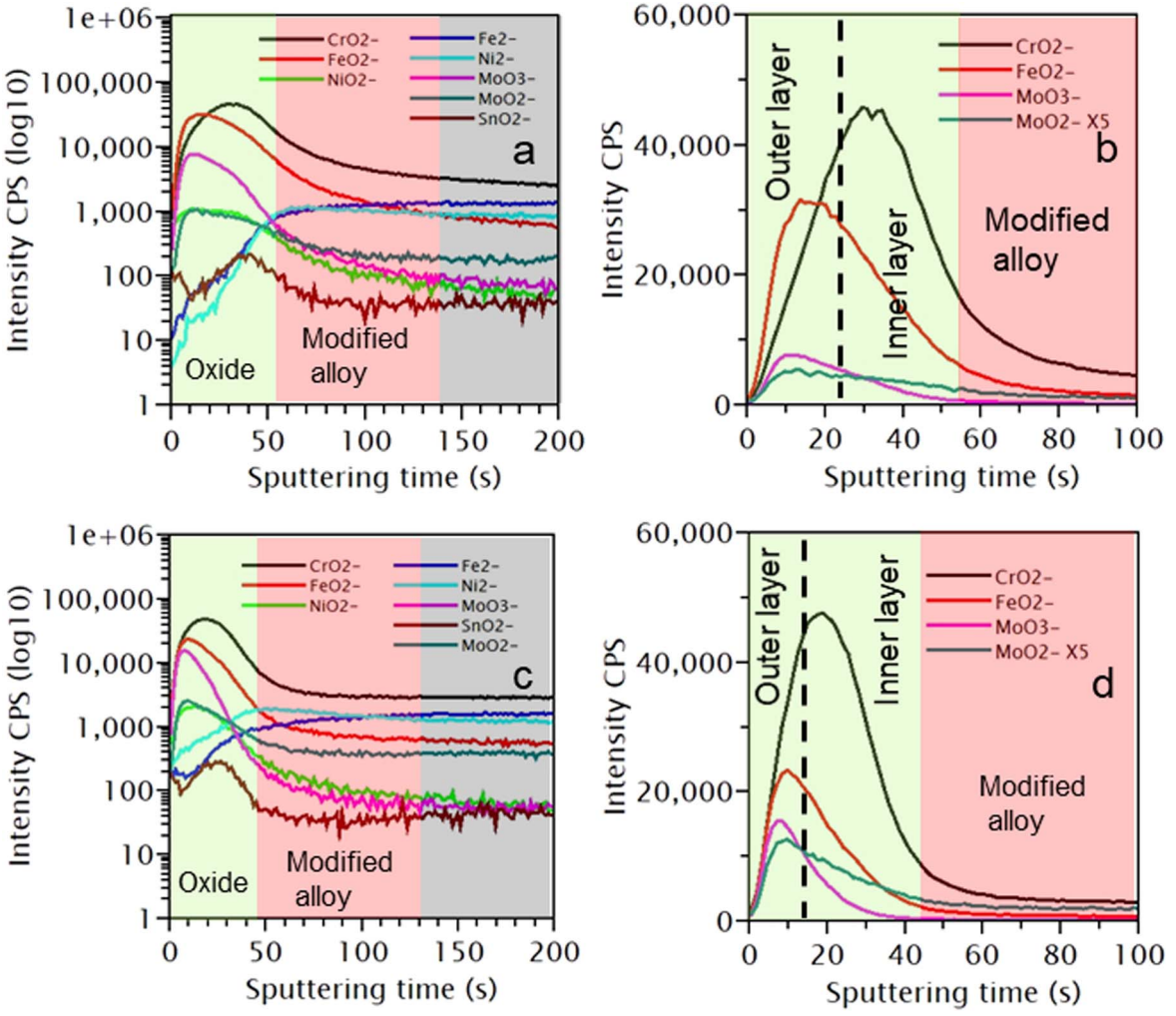

Figure 2. ToF-SIMS depth profiles of selected negative ions for (a), (b) TP and (c), (d) VP SS316L samples.

HTA samples showed the same characteristic features, so only the TP + HTA surface is presented in Figs. 1e, 1f (VP + HTA sample is presented in the supplementary material, Fig. S1 (available online at stacks.iop.org/JES/169/011505/mmedia)). The grain boundaries are now clearly revealed, making the grains well distinct both in the OM and AFM images. This is because of the restructuring of the surface made possible by long-range atomic transport at high temperatures. At the topmost surface observed by AFM (Figs. 1f, S1b), the absence of polishing lines shows that the surface stress has been fully relaxed and the cold work layer fully restructured by the annealing treatment. The microstructure is now clearly revealed, including at the topmost surface.

Native oxide film characterization.— *ToF-SIMS depth profiling.*—The secondary ions considered for ToF-SIMS depth profile analysis were Fe_2^-, Ni_2^-, FeO_2^-, CrO_2^-, NiO_2^-, MoO_3^-, MoO_2^- and SnO_2^-. The FeO_2^-, CrO_2^-, NiO_2^- MoO_3^-, MoO_2^- and SnO_2^- ions are characteristic for oxidized species in the surface oxide film, and the Fe_2^- and Ni_2^- ions for fragments mainly originating from the metal substrate. Both MoO_3^- and MoO_2^- ions were selected in an attempt to discriminate Mo(VI) and Mo(IV) oxide species, respectively. The SnO_2^- ions were selected because of Sn contamination, more notably observed at the surface after high-temperature annealing because of segregation from the bulk. The intensities of the secondary ions are reported either using a logarithmic scale, which puts emphasis on signals of low intensity, or using a linear scale. The ion intensities depend on the ion emitter matrix, but their variations with sputtering time reflect the variation of the in-depth elemental concentration when emitted from the oxide matrix or metal matrix. The metal/oxide interface was positioned at a sputtering time corresponding to approximately 80% of the maximum intensity of the Ni_2^- signal as previously proposed.[52]

Figure 2 compares ToF-SIMS depth profiles obtained for the TP and VP samples. For the TP sample (Fig. 2a), the Ni_2^- profile analysis allows us to locate the metal/oxide interface at around 52 s of sputtering time, meaning that the oxide film region extends from 0 to ~52 s and the substrate alloy region beyond. The sputtering time from ~52 to ~140 s is considered as the Ni-enriched modified alloy region typically found on Ni-containing stainless steels.[11,22,31,32,48,52] In the oxide film region (enlarged in Fig. 2b and with intensities reported in linear scale), the CrO_2^- and FeO_2^- signals are the most intense, followed by the MoO_3^- signal. The MoO_2^- signal has a lower intensity than the MoO_3^- signal and displays a different profile, indicating that the MoO_2^- ions are sub-fragments originating from Mo(VI) oxide species and main fragments originating from Mo(IV) oxide species. The NiO_2^- and SnO_2^- ions are much less intense (Fig. 2a), suggesting that oxidized nickel and oxidized tin are at trace level in the oxide film, as confirmed by the XPS analysis discussed below. The traces of oxidized tin are concentrated in the inner part of the oxide region at the interface with the alloy substrate, whereas those of oxidized nickel are more homogeneously distributed in the depth of the oxide film.

The MoO_3^- and FeO_2^- profiles peak at ~11 and ~15 s, respectively, and the CrO_2^- profile later at ~30 s of sputtering time (Fig. 2b). This is clear evidence that the native oxide layer covering the TP surface has a bilayer structure with oxidized iron and molybdenum concentrated in the outer layer and oxidized chromium

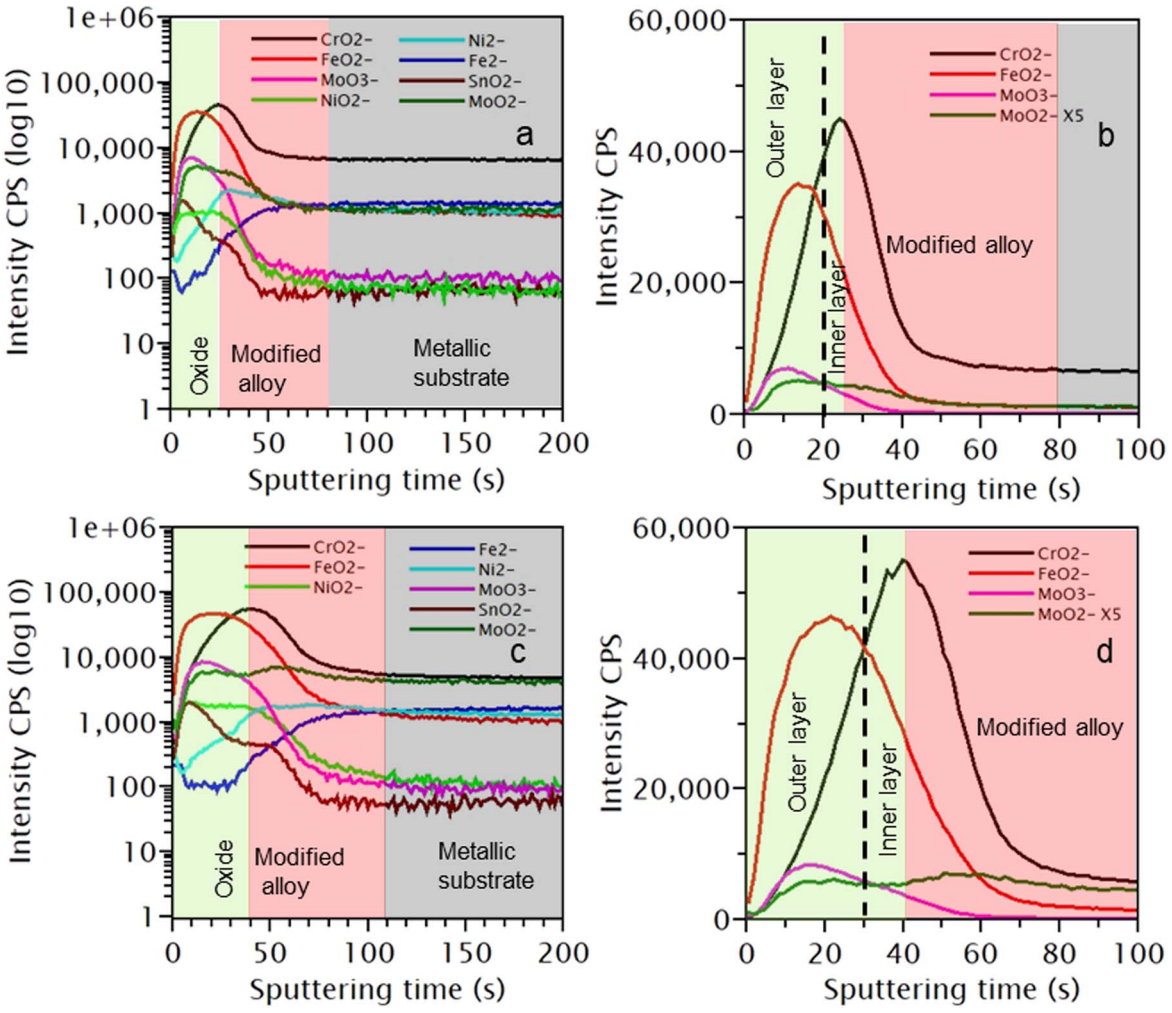

Figure 3. ToF-SIMS depth profiles of selected negative ions for (a), (b) TP + HTA and (c), (d) VP + HTA SS316L samples.

concentrated in the inner layer, as previously observed.[11,22,30–32,48] The interface between the outer and inner oxide layers can be located at ~23 s, based on the median sputtering time between the intensity maxima of the FeO_2^- and CrO_2^- profiles.[48] This partition in the distribution of the main oxidized species film is also illustrated by the profile of the CrO_2^-/FeO_2^- intensity ratio that continuously increases until the end of the oxide region and levels off afterward (see Fig. S2a in supplementary material). The MoO_2^- profile also peaks in the outer layer but less steeply decreases in the inner layer than the MoO_3^- profile, suggesting that the Mo(IV) species could be more homogeneously distributed in-depth than the Mo(VI) species.

For the VP sample (Figs. 2c, 2d), the interface between the oxide layer and modified alloy region can be positioned at ~45 s of sputtering time using the same method as for the TP sample. The MoO_3^-, FeO_2^-, and CrO_2^- signals peak sequentially from the outer surface, like for the TP surface, but sooner at 8, 9, and 18 s, respectively, showing that although possibly thinner, the native oxide film develops a similar bilayer structure. The separation of the outer and inner oxide layer is at ~14 s, considering the median sputtering time of the FeO_2^-, and CrO_2^- maxima. Comparison of Fig. 2d with Fig. 2b shows markedly higher and lower intensities for the MoO_3^- and FeO_2^- ions, respectively, for the VP sample, whereas the CrO_2^- ions intensity is slightly higher. Clearly, this suggests Fe depletion balanced by Mo and Cr enrichments in the native oxide film on the VP sample compared to the TP sample. Higher Cr/Fe balance in the oxide film is confirmed by the higher CrO_2^-/FeO_2^- intensity ratio reached at the oxide/alloy interface (Fig. S2b in supplementary material). Like for the TP sample, the MoO_2^- profile less steeply decreases in the inner oxide region than the MoO_3^- profile. Mo(IV) species would be more concentrated than Mo(VI) species in the inner layer in the native oxide film obtained from the VP finishing process. The NiO_2^- and SnO_2^- ions profiles have the same characteristics as for the TP sample.

Figures 3a, 3b presents the ToF-SIMS depth profiles obtained for a TP surface submitted to high-temperature annealing (TP + HTA sample). Using the same method for positioning the oxide/metal interface, we obtain a value of ~24 s, much lower than for the TP sample. However, we note in Fig. 3a that the Ni_2^- profile peaks nearly simultaneously with the CrO_2^- profile, whereas the peaks were well separated for the TP sample. This suggests that intermixing between oxidized chromium and metallic nickel occurred, possibly during the annealing treatment. Our explanation is that chromium oxide was not fully reduced in the gaseous hydrogen environment at high temperature—annealing time would need to be optimized for full reduction—resulting in the formation of an interdiffusion layer above which the native oxide subsequently developed. As better seen in Fig. 3b, the MoO_3^-, FeO_2^- and CrO_2^- signals peak sequentially, like for the TP and VP samples, pointing to a similar bilayer chemical structure. The separation between the outer and inner oxide layer is at ~20 s, adopting the same methodology as above, close to the value obtained for the TP sample. The MoO_3^-, FeO_2^- and CrO_2^- intensities reach similar maxima as for the TP sample, suggesting no pronounced Cr/Mo/Fe balance variations in the oxide film after the HTA surface finish. Similar Cr/Fe balance as after TP finish is confirmed by the CrO_2^-/FeO_2^- intensity ratio reached at the oxide/alloy interface (Fig. S3a in supplementary material). Like for the TP sample, the MoO_2^- profile less steeply decreases in the inner layer than the MoO_3^- profile. In contrast with the TP sample, the SnO_2^- profile peaks at a higher intensity and at the top of the oxide film after annealing. This suggests the atomic transport of tin across the oxide film after its segregation on the surface at high temperatures.

For the VP + HTA sample (Figs. 3c, 3d), the maximum of the MoO_3^-, FeO_2^-, and CrO_2^- intensity profiles is at ~17, ~22, and ~40 s, respectively, more than twice the values obtained for the VP sample, which suggests a thicker native oxide film than on the VP sample. The interface between the outer oxide layer and the inner oxide layer is positioned at 31 s. The interface between the oxide film and metal substrate is at ~40 s, adopting the same procedure as above. However, like for the TP + HTA sample, it coincides with the maxima of the CrO_2^- profile, also pointing to the formation of an interdiffusion layer. Tin oxide is also accumulated in the outer part of the oxide film, and oxidized nickel is homogeneously distributed across the oxide film. The relative intensity maxima of the MoO_3^-, FeO_2^-, and CrO_2^- profiles are similar to those obtained with the TP and TP + HTA samples, suggesting chromium and molybdenum enrichments in the native oxide film that are similar as after TP or TP + HTA surface finish but lower than after VP surface finish. Like for all other samples, the MoO_2^- profile less steeply decreases in the inner layer than the MoO_3^- profile and even peaks in the interdiffusion region, pointing to a more homogeneous in-depth distribution of Mo(IV) compared to Mo(VI) oxide species.

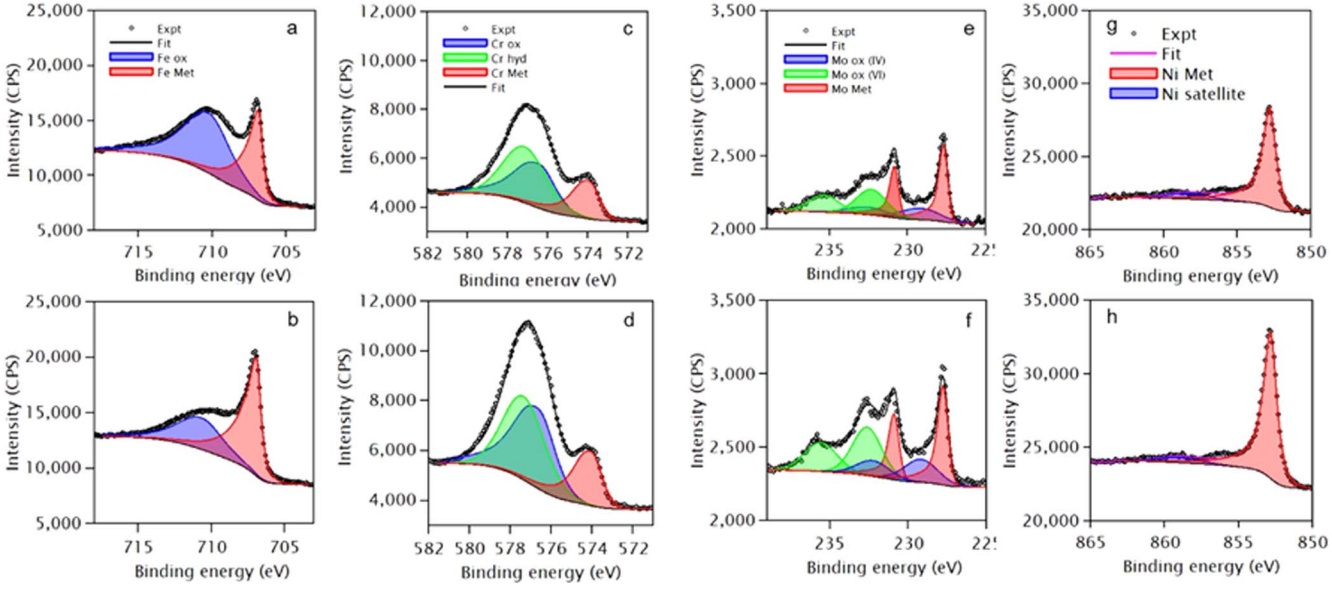

Figure 4. XPS high resolution spectra and peak fitting of (a), (b) Fe 2p3/2, (c), (d) Cr 2p3/2, (e), (f) Mo 3d and (g), (h) Ni 2p3/2 core-levels for (a), (c), (e), (g) TP and (b), (d), (f), (h) VP SS316L samples.

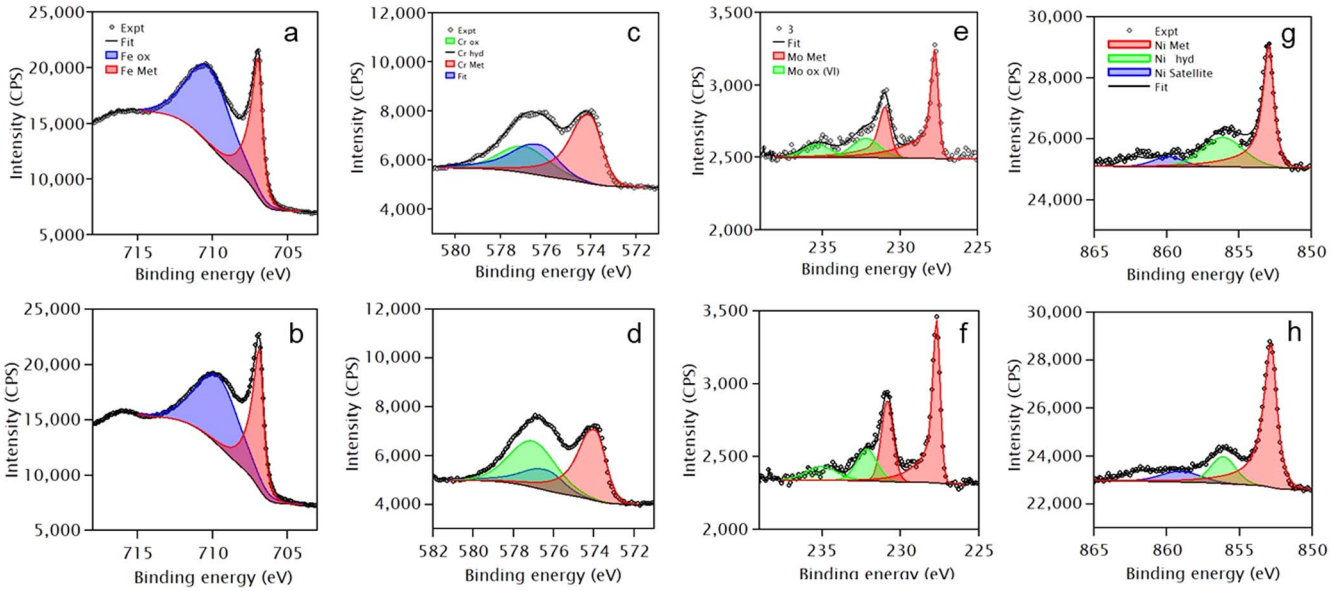

Figure 5. XPS high resolution spectra and peak fitting of (a), (b) Fe 2p3/2, (c), (d) Cr 2p3/2, (e), (f) Mo 3d and (g), (h) Ni 2p3/2 core-levels for (a), (c), (e), (g) TP + HTA and (b), (d), (f), (h) VP + HTA SS316L samples.

XPS analysis.—Figure 4 presents the Fe 2p3/2, Cr 2p3/2, Mo 3d, and Ni 2p3/2 high-resolution core-level spectra obtained after TP and VP surface finish, and Fig. 5 those obtained on samples submitted to the HTA treatment (TP + HTA and VP + HTA samples). The BE, FWHM, and RI (relative intensity) values obtained by peak fitting are listed in Table I.

For the TP and VP samples (Fig. 4, Table I), the peaks at 706.8 and 710.2/710.6 eV in the Fe 2p3/2 spectra were assigned to a Fe^0 (metal) component and a generic Fe^{3+} (hydroxide/oxide/oxyhydroxide) component, respectively.[51] The generic component assigned to Fe^{3+} is broad, suggesting that it may also correspond to ferrous species. For the VP sample, we note a positive BE shift of the Fe^{3+} component indicative of a change in the oxide matrix. We also note a marked decrease in relative intensity, indicating, in agreement with the trend observed by ToF-SIMS, that oxidized iron is markedly less present at the surface than on the TP sample. In the Cr 2p3/2 spectra, the peak components at 573.9/574, 576.4/576.6 and 577.1/577.3 eV were assigned to Cr^0 (metal), Cr^{3+} (oxide) and Cr^{3+} (hydroxide), respectively.[51] For the VP sample, the total relative intensity of the oxide and hydroxide components is slightly increased (80.2%) compared to the TP sample (78.5%), suggesting a slight increase in Cr^{3+} oxidized species at the surface. The hydroxide/oxide balance favors oxide after the VP finish and hydroxide after the TP finish, suggesting that VP finishing is less favorable to hydroxylation.

The Mo 3d spectra were reconstructed with 5/2–3/2 spin doublets of fixed intensity ratio. The 3d 5/2 components at 227.6/227.7, 229.1 and 232.2/232.1 eV for the TP/VP samples were assigned to Mo^0 (metal), Mo^{4+} (oxide), and Mo^{6+} (oxide), respectively.[22,30,31,34] We note a change in broadness of the minority component assigned to Mo^{4+}. The Mo^{4+}/Mo^{6+} intensity ratio is 0.38 and 0.53 for the TP and VP samples, respectively, indicating the predominance of Mo^{6+} species in both cases and its decrease after VP finish. Considering total oxidized molybdenum, its relative intensity increases after VP finish (63.3%) compared to TP finish (54%), also in good agreement with the trend observed by ToF-SIMS.

Only the metallic component with its satellite was used for fitting the Ni 2p3/2 core-level spectra for the TP and VP samples. No tin was observed. This indicates that the trace level of oxidized species detected by ToF-SIMS for both elements is below the detection limit of XPS. The O 1 s core-level spectra for the TP and VP samples are presented in the supplementary material (Fig. S4). They were fitted with three components at 530.2/530.1, 531.6, and 532.5/532.3 eV assigned to oxide (O_2^-), hydroxide (OH^-), and water (H_2O) ligands in the oxide film, respectively.[7,22,51,53] The latter component can also correspond to surface contamination, including double-bonded oxygen. The OH^-/O_2^- intensity ratio is 1.2 for the TP surface and 1.1 for the VP surface, suggesting slight dehydroxylation after the VP finish in agreement with the decrease in relative intensity of the Cr^{3+} (hydroxide) component.

For the TP + HTA and VP + HTA samples (Fig. 5, Table I), the peak components and their assignment are the same as for the TP and VP samples, showing the presence of the same surface species. Additional components were observed at 856.1 eV and 486.7 eV and assigned to Ni^{2+} (hydroxide) and Sn^{4+} (oxide) species, respectively. The Fe^{3+} relative intensities are 63.4 and 60.2% for the TP + HTA and VP + HTA samples compared to 63.6 and 37.5% for the TP and VP samples, respectively, showing no effect of the HTA treatment on the TP samples, whereas the marked decrease in iron oxide observed at the surface after VP finish is no longer observed after HTA finish. Cr^{3+} oxide and hydroxide species are present on TP + HTA and VP + HTA surfaces, with Cr^{3+} hydroxide predominant on the VP + HTA sample. The Cr^{+3}(hyd)/Cr^{+3}(ox) intensity ratios are 0.8 and 2.3 for the TP + HTA and VP + HTA samples, respectively, compared to 1.2 and 0.9 for the TP and VP samples, respectively. The trend to dehydroxylation observed after VP finish is no longer observed after subsequent HTA finish. In the case of molybdenum, only Mo^{6+} oxide is observed on both TP + HTA and VP + HTA surfaces. Total oxidized molybdenum has a relative intensity of 38 and 26.3% vs 69.1 and 61.8% for the TP and VP samples, respectively, indicating much less oxidized molybdenum present at the surface after HTA finish and suggesting a detrimental effect of HTA finish for promoting Mo enrichment in the native film. The additional components needed for fitting the Ni 2p3/2 spectra correspond to Ni^{2+} hydroxide[1,28,31,51] and its satellite.[36,54] More Ni^{2+} hydroxide species would form after treating the TP surface with HTA finish than after treating the VP surface. In the Sn 3d5/2 spectra (Fig. S5 in supplementary material), only one component assigned to Sn^{4+} oxide was observed[55] in agreement with the ToF-SIMS data that show the formation of tin oxide in the outer part of the oxide layer. The O 1 s spectra (Fig. S5 in supplementary material) were fitted with the same peak components assigned to O_2^-, OH^- and H_2O ligands. The OH^-/O_2^- intensity ratio is 0.7 for the TP + HTA surface and 0.5 for the VP + HTA surface, showing reduced hydroxylation of the native oxide films after HTA finish for TP (1.2) and VP (1.1) surfaces.

Film thickness and surface composition.—The relative intensities obtained by peak fitting of the XPS spectra were used to calculate

Table I. Binding energy (BE), full width at half maximum (FWHM), and relative intensity (RI) of component peaks obtained from reconstruction of XPS core-level spectra for TP, VP, TP + HTA, and VP + HTA SS316L samples.

			TP			VP			TP + HTA			VP + HTA		
Core level	Peak	Assignment	BE (±0.1 eV)	FWHM (±0.1 eV)	RI (±0.5%)	BE (±0.1 eV)	FWHM (±0.1 eV)	RI (±0.5%)	BE (±0.1 eV)	FWHM ±0.1 eV)	RI (±0.5%)	BE (±0.1 eV)	FWHM (±0.1 eV)	RI (±0.5%)
Fe 2p3/2	Fe^{0}	Metal	706.8	0.6	36.3	706.8	0.6	62.4	706.9	0.6	36.5	706.8	0.6	39.7
	Fe^{3+}	Oxide	710.2	3.5	63.6	710.6	3.5	37.5	710.1	3.5	63.4	710	3.5	60.2
Cr 2p3/2	Cr^{0}	Metal	573.9	1.31	21.5	574	1.31	19.7	574	1.31	46	573.9	1.31	42.5
	Cr^{3+}	Oxide	576.4	2	35.3	576.6	2	41.3	576.2	2	29.6	576.3	2	17.3
	Cr^{3+}	Hydroxide	577.1	2.5	43.2	577.3	2.5	38.9	577	2.5	24.2	577	2.5	40
Mo 3d5/2	Mo^{0}	Metal	227.6	0.76	46	227.7	0.76	37.7	227.7	0.76	62	227.5	0.76	73.6
	Mo^{4+}	Oxide	229.1	3.2	14.8	229.1	2.6	21.8	—	—	—	—	—	—
	Mo^{6+}	Oxide	232.2	2.2	39.2	232.1	2.2	40.5	232.2	2.2	38	232.2	2.2	26.3
Ni 2p3/2	Ni^{0}	Metal	852.7	1.01	89	852.8	1.01	93	852.9	1.01	57	852.8	1.01	71
	Ni^{2+}	Hydroxide	—	—	—	—	—	—	856.1	2.1	35	856.1	2.1	18
	Ni^{0}	Satellite	859	3.5	11	859	3.5	7	859.8	3.5	8	859.8	3.5	11
O 1 s	O_2^{-}	Oxide	530.2	1.2	34.1	530.1	1.2	27.7	530.3	1.0	30.6	530.2	1.0	47.9
	OH^{-}	Hydroxide	531.6	1.5	41.2	531.6	1.5	30.7	531.2	1.4	21.3	531.2	1.4	22.6
	H_2O	water	532.5	2.6	24.6	532.3	2.6	41.5	532.5	2.2	48	532.2	2.2	29.4
Sn 3d5/2	Sn^{4+}	Oxide	—	—	—	—	—	—	486.7	1.1	100	486.7	1.2	100

the oxide film thickness and surface composition based on single-layer and bilayer models of the attenuation of the photoelectrons intensities.[22,30–32,34,51] The single-layer model assumes a homogeneous in-depth distribution of all oxide and hydroxide species in an oxide film of uniform thickness over an alloy substrate of uniform but modified composition compared to the bulk alloy. The values obtained for the thickness of the oxide film, its relative concentration in alloying elements and that of the modified alloy region underneath the oxide film are presented in Table II.

The oxide layer ranges from 1.4–2.0 nm in thickness for all four cases, in good agreement with values reported for native films formed in ambient air on stainless steel.[11,52,54] For the TP sample, oxide thickness is 1.4 nm, with iron oxide being the major constituent (58%). Total oxidized chromium (Cr^{3+} oxide and hydroxide) is 39%, confirming the enrichment of this element in the native oxide film obtained from the traditional surface finish by mechanical polishing compared to the bulk concentration of 20% in the alloy.[22,51] The remaining 3% of an alloying element corresponds to oxidized molybdenum (Mo^{4+} and Mo^{6+}), a value suggesting some enrichment compared to the bulk alloy, but that should be taken with caution given the uncertainty. Consistently, the modified alloy underneath the oxide film is found depleted in chromium (enriched in the oxide) and enriched in nickel (below the detection limit in the oxide), the latter in agreement with the ToF-SIMS data. Metallic molybdenum is found at its bulk value.

After vibratory surface finishing, the native oxide layer thickness is found to be 1.3 nm, similar to that found after TP surface finishing, but the surface composition is different. The relative concentration of oxidized iron is about half that measured after TP finishing, confirming the marked decrease observed by ToF-SIMS. This decrease in iron oxide is balanced by increasing the enrichment in chromium and molybdenum in the oxide film, both elements being about twice as concentrated than after TP finishing. In the modified alloy, Ni is further enriched compared to TP finishing, mostly due to the preferential consumption of iron by the vibratory finishing process. Metallic Cr and Mo are at about the same concentration as after TP finishing. These results indicate a pronounced effect of the vibratory finishing process on the surface composition. Iron is preferentially consumed, possibly by a mechanism of preferential erosion corrosion, resulting in a marked increase in the enrichment of Cr and Mo in the oxide film and Ni in the modified alloy. The beneficial effect on the enrichment of the native oxide in Cr and Mo can improve the corrosion resistance in an aggressive environment, as confirmed by the electrochemical analysis below.

For the TP + HTA and VP + HTA samples, the native oxide film thickness is 2.0 and 1.8 nm, respectively, suggesting the formation of thicker films than after TP or VP surface finishing. The oxide film composition on the TP + HTA and VP + HTA samples is found to be very similar. It is dominated by oxidized iron, like after TP finishing, with oxidized nickel and oxidized tin being additionally present, independently of the initial differences found after TP and VP finishing. This evolution is consistent with the native oxides formed after TP or VP finishing being reduced in the hydrogen environment during high-temperature annealing and fresh native oxide films being reformed after subsequent exposure of the HTA-treated samples to ambient air. In this way, the beneficial effect of VP finishing on the surface enrichment in chromium and molybdenum oxides is lost, and the Fe/Cr/Mo balance in the native oxide films is close to that obtained after TP finishing. In the modified alloy region, both the TP + HTA and VP + HTA samples remain enriched in metallic nickel but at lower concentrations than on the respective TP and VP samples owing to the consumption of this element upon the reformation of the native oxides. Metallic chromium initially depleted in the TP and VP samples is more concentrated, which is assigned to segregation from the bulk during the high-temperature annealing in reducing conditions.[28,34] Mo would be slightly enriched compared to the initial TP and VP samples, but this should be taken with caution given the uncertainty. The slight enrichment in Cr and possibly Mo of the modified alloy region could benefit the self-repair properties of the oxide film in aggressive environments.

A bilayer model, based on the stratified chemical surface structure observed by ToF-SIMS, was also applied to more precisely describe oxide film thickness and composition. In this case, an inner layer consisting only of Cr^{3+} oxide was considered, and all other oxides and hydroxide species were considered homogeneously distributed in the depth of the outer layer.[30–32,34,35,48] The bilayer model is consistent with forming an inner chromium oxide barrier between the outer (hydr)oxide layer of ion exchange with the environment and the alloy substrate.[30–32,34,48] The minor concentrations of the inner barrier layer in iron and molybdenum oxide species suggested by the ToF-SIMS depth profiles were neglected. Results are shown in Table III. Concentration values for the modified alloy region are identical within the uncertainty to those reported in Table II and are not repeated in Table III. The relative concentration of the inner oxide layer in alloying elements is not tabulated as it is assumed in the model to be 100% Cr^{3+} oxide. For the outer layer, the relative concentration is that of Fe^{3+} oxide, Cr^{3+} hydroxide, and $Mo^{4+/6+}$ oxide for the TP and VP samples. For the TP + HTA and VP + HTA samples, Ni^{2+} hydroxide and Sn^{4+} oxide are also taken into account.

For the TP sample, the total oxide film thickness is 1.7 nm with this model, including a 1.2 nm thick outer layer and a 0.5 nm thick inner layer, in good agreement with values also obtained with a bilayer model for native oxides formed on SS316L surfaces prepared with TP surface finishing.[22,32,48] The outer layer of the oxide film mostly consists of Fe^{3+} oxide (78%), Cr^{3+} hydroxide (20%) and $Mo^{4+/6+}$ oxide (2%) being as concentrated as in the bulk alloy. The Cr^{3+} enrichment found with the single-layer model is concentrated in the 0.5 nm thick inner oxide layer.

For the VP sample, the total thickness of the oxide film is found slightly lower (1.5 vs 1.7 nm), however including a thinner (0.8 vs 1.2 nm) outer layer and a thicker (0.7 vs 0.5 nm) inner layer. Compared to the TP sample, the increase in Cr^{3+} enrichment found with the single-layer model is reflected by the increase of the inner layer thickness and the increase of the Cr^{3+} hydroxide concentration (39 vs 20%) in the outer layer. The ToF-SIMS depth profiles revealed this feature as the CrO_2^- maximum shifted towards the outer layer (Figs. 2b, 2d). Considering the increase in $Mo^{4+/6+}$ enrichment, it is confirmed by the increase in $Mo^{4+/6+}$ oxide (5 vs

Table II. Surface composition and oxide layer thickness as calculated from the XPS data with a single-layer model of photoelectron attenuation.

		Relative concentration (±2 at%)								
		Oxide film					Modified alloy			
Surface finish	Thickness (±0.1 nm)	Fe	Cr	Mo	Ni	Sn	Fe	Cr	Ni	Mo
TP	1.4	58	39	3	—	—	63	10	25	2
VP	1.3	30	63	7	—	—	50	13	35	2
TP + HTA	2.0	60	22	2	6	10	54	23	20	3
VP + HTA	1.8	55	27	2	4	11	47	21	28	4

Table III. Oxide layer thickness and composition as calculated from the XPS data with a bilayer model. The composition of the inner layer is 100% Cr oxide.

	Thickness (±0.1 nm)			Relative concentration of outer oxide layer (±2%)				
Stage	Total	Outer layer	Inner layer	Fe	Cr	Mo	Ni	Sn
TP	1.7	1.2	0.5	78	20	2	—	—
VP	1.5	0.8	0.7	56	39	5	—	—
TP + HTA	1.7	1.3	0.4	61	7	1	8	23
VP + HTA	1.6	1.3	0.3	54	13	1	6	25

2%) in the outer layer. These results emphasize that vibratory surface finishing promotes the formation of a slightly thicker chromium oxide inner barrier layer and chromium hydroxide and molybdenum oxide enrichment in the outer exchange layer, likely due to preferential etching of iron.

For the TP + HTA and VP + HTA samples, the thickness of the inner and outer layers and composition of the outer layer are similar and closer to those of the TP finished surface than to the VP finished surface. The loss in the Cr^{3+} enrichment in the VP sample is reflected by the formation of a thinner inner layer (0.3 vs 0.7 nm) and a marked decrease of the Cr^{3+} hydroxide concentration in the outer layer (13 vs 39%) of the VP + HTA sample. The loss in the $Mo^{4+/6+}$ enrichment in the outer layer is also pronounced (1 vs 5%), although attenuated by the outer layer thickness increase (1.3 vs 0.8 nm). Ni^{2+} hydroxide and Sn^{4+} oxide are found at a similar concentration in the outer layer of the oxide films on HTA samples independently of the initial TP or VP treatment.

Passivity and corrosion resistance.—Figure 6 shows the potentiodynamic polarization curves recorded in 0.05 M H_2SO_4(aq) after 30 min stabilization at OCP for SS316L samples with TP, VP, TP + HTA, or VP + HTA surface finish. For the TP, TP + HTA, and VP + HTA samples, corrosion potentials are similar at $U_{corr} = -0.45 \pm 0.01$, -0.44 ± 0.01 and -0.43 ± 0.01 V_{SHE}, respectively. The cathodic branches do not show any marked differences suggesting similar proton reduction properties in the acid electrolyte. Also, the anodic branches are nearly superimposed indicating a similar passivation behavior and an active-passive transition marked by a small activation peak. During stabilization at OCP, Fe^{3+} oxide preferentially dissolves, as shown previously,[22,30,31] promoting Cr^{3+} (hydr)oxide and $Mo^{4+/6+}$ oxides enrichment. For the TP + HTA and VP + HTA samples, it is expected that Ni^{2+} hydroxide and Sn^{4+} oxide also dissolve at OCP. Thus, the small initial differences in surface composition of these samples are attenuated, resulting in no marked variations of the surface reactivity and passivation properties.

For the VP sample, the corrosion potential is less negative at $U_{corr} = -0.36 \pm 0.01$ V_{SHE}, showing the more noble character provided by native oxide film further enriched in chromium and molybdenum as shown by surface analysis. Also, the current is notably lower in the active-passive transition range between U_{corr} and $U_{corr} + 0.5$ V, with no activation peak observed. These differences show that even after stabilization at OCP, which promotes Cr and Mo enrichment in the surface oxide film, the initial enrichments of these two elements brought by VP surface finishing have a beneficial effect on the corrosion resistance by improving the resistance to dissolution at the active-passive transition. As the potential increases in the passive domain, the observed differences in anodic current between the VP and other samples are attenuated, which we assign to the increasing dissolution of chromium as the transpassive domain is approached.[22,30,31] Thus, the beneficial effect brought by vibratory finishing in the lower potential range of passivity is progressively lost upon increasing anodic polarization.

Figure 7 compares the anodic passivation current transients obtained for the TP and VP samples in 0.05 M H_2SO_4(aq) at +0.3 V_{SHE} with step-wise addition of Cl^- ion in the base electrolyte as marked. Since the TP + HTA and VP + HTA samples showed similar passivation behavior as the TP sample, the VP sample is only compared with the TP sample. The semi-log plot shows that the current density drops rapidly and then levels off continuously during the first 60 min of passivation in the Cl-free base electrolyte. This behavior shows that the passive film becomes increasingly protective with time, however, without reaching a stable steady-state. It is typical of austenitic stainless steel[22] and in agreement with previous studies performed with ultra-low current measurement setups and micrometer-sized electrodes, where a stable steady-state of passivity took extremely long to attain.[37] We assign the instabilities observed for the VP sample to the electronic noise of the setup captured in the

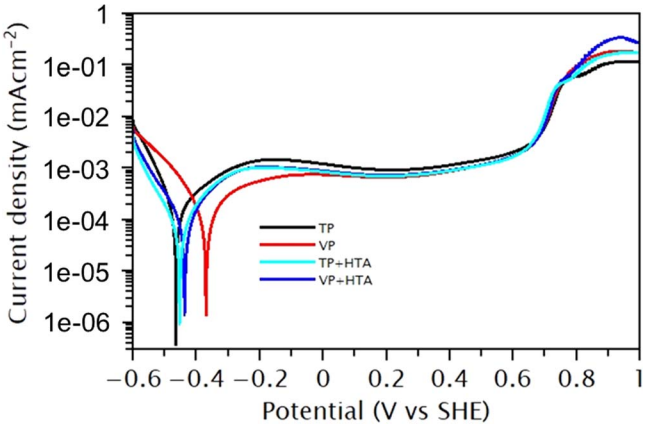

Figure 6. Polarization curves of SS316L samples with TP, VP, TP + HTA, and VP + HTA surface finish recorded in 0.05 M H_2SO_4(aq) after 30 min stabilization at OCP (scan rate: 1 mV s^{-1}).

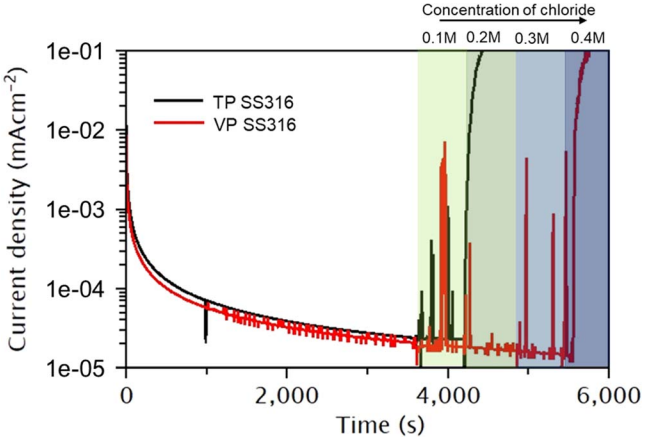

Figure 7. Passivation current transients for TP and VP samples in 0.05 M H_2SO_4(aq) after 15 min stabilization at OCP. Samples were polarized at +0.3 V_{SHE} in the Cl-free base electrolyte before step-wise addition of chloride ions every 10 min as marked.

lowest current ranges on this particular experiment. All along the experiment, a slightly lower current density is observed for the VP sample, in agreement with the trend also shown by the polarization curves. This difference is maintained even after the addition of chlorides. It shows that the near steady-state of passivity obtained with VP finishing is slightly more protective against generalized corrosion than that obtained with TP finishing. We assign this effect to the higher Cr enrichment, forming a thicker inner barrier layer in the initial native oxide obtained after vibratory finishing.

After the addition of chlorides, we observe anodic current spikes indicative of depassivation/re-passivation events. Figure S6 in supplementary material shows a zoomed-in region between 3750 and 3850 s of the current transient for the TP sample. The slower increase of current in the spikes represents anodic dissolution during initial pit growth after local passivity breakdown, and the rapid drop-down indicates the re-passivation of the pit by self-repair.[56,57] These features correspond to metastable pitting events. Transient initiation of crevices cannot be excluded despite the conditions of anodic polarization of the experiment.

For the TP sample, four of such metastable events are observed after the addition of 0.1 M NaCl, indicating that the passive film is susceptible to breakdown but does self-repair. As soon as the chloride concentration increases to 0.2 M, the current steeply increases but does not drop down, indicating passivity breakdown and the failure of self-repair leading to localized corrosion. For the VP sample, only one metastable event is observed after adding 0.1 M NaCl, indicating increased resistance of the passive film to breakdown. Even after reaching a higher metastable pitting current than for the TP sample, re-passivation is observed. At chloride concentration of 0.2 M and 0.3 M, three more metastable events are observed with some of them reaching higher currents than for the TP sample. This confirms the improved resistance to breakdown provided by vibratory surface finishing. Only at the chloride concentration of 0.4 M failure of self-repair leading to the initiation of localized corrosion is observed after one more metastable event. We assign the improved resistance to breakdown obtained with the VP surface finish to the increased Cr and Mo enrichment in the initial native oxide formed on the surface. Both elements would contribute to strengthen the Fe-rich weak sites of passivity of the oxide film formed after anodic passivation, thus reinforcing the stability of the passive film and its resistance to chloride-induced breakdown.

Conclusion

Surface and electrochemical analysis were combined to study the effects of surface finishing by mechanical polishing, vibratory polishing, or high-temperature annealing on the topology and composition of the native oxide-covered surface of 316L stainless steel and the passivation behavior in aggressive acid electrolyte and resistance to chloride-induced localized corrosion.

Compared to traditional surface finishing by mechanical polishing, vibratory finishing improves the surface topology by partially removing the cold-worked layer without revealing the bulk structure at the topmost surface. Vibratory finishing effectively promoted passivity, as shown by the current density decrease observed at the active-passive transition and in the near steady-state of passivity. Resistance to chloride-induced passivity breakdown is improved, as shown by the decrease of metastable events and increase of chloride concentration needed to trigger stable pitting/crevice corrosion. Vibratory finishing increases the Cr and Mo enrichments in the native oxide film. As a result, the bilayer structure is characterized by a thicker Cr^{3+} oxide inner barrier layer and a more Cr^{3+} hydroxide- and $Mo^{4+/6+}$ oxides-enriched outer exchange layer. These enhanced Cr and Mo enrichments are thought to reinforce the Fe-rich weak sites of passivity against chloride-induced breakdown.

High-temperature annealing under reducing gas is quite effective in fully reconstructing the cold-worked layer produced by mechanical polishing owing to promoted long-range atomic mobility, which allows revealing the bulk microstructure at the topmost surface. However, the native oxide film formed at the surface develops a bilayer structure with similar Cr and Mo enrichments as after classical mechanical polishing. The improved Cr and Mo enrichments obtained with vibratory polishing are lost after subsequent high-temperature annealing, and, consistently, the passivation behavior is similar to that observed with traditional mechanical polishing.

Acknowledgments

This project has received funding from the European Research Council (ERC) under the European Union's Horizon 2020 research and innovation program (ERC Advanced grant no. 741123).

ORCID

Vincent Maurice https://orcid.org/0000-0001-5222-9972
Philippe Marcus https://orcid.org/0000-0002-9140-0047

References

1. V. Maurice and P. Marcus, "Progress in corrosion science at atomic and nanometric scales." *Prog. Mater Sci.*, **95**, 132 (2018).
2. V. Maurice, W. P. Yang, and P. Marcus, "XPS and STM study of passive films formed on Fe-22Cr(110) single-crystal surfaces." *J. Electrochem. Soc.*, **143**, 1182 (1996).
3. M. Seo and N. Sato, "Differential composition profiles in depth of thin anodic oxide films on iron-chromium alloy." *Surf. Sci.*, **86**, 601 (1979).
4. G. Hultquist, M. Seo, T. Leitner, C. Leygraf, and N. Satot, "The dissolution behavior of iron, chromium, molybdenum and copper from pure metals and from ferritic stainless steels." *Corros. Sci.*, **27**, 937 (1987).
5. S. Mischler, H. J. Mathieu, and D. Landolt, "Investigation of a passive film on an iron-chromium alloy by AES and XPS." *Surf. Interface Anal.*, **1**, 182 (1988).
6. P. Marcus and I. Olefjord, "A round robin on combined electrochemical and AES/ESCA characterization of the passive films on Fe-Cr and Fe-Cr-Mo alloys." *Corros. Sci.*, **28**, 589 (1988).
7. J. E. Castle and J. H. Qiu, "A co-ordinated study of the passivation of alloy steels by plasma source mass spectrometry and X-ray photoelectron spectroscopy—1. characterization of the passive film." *Corros. Sci.*, **29**, 605 (1989).
8. W. P. Yang, D. Costa, and P. Marcus, "Resistance to pitting and chemical composition of passive films of a Fe-17%Cr alloy in chloride-containing acid solution." *J. Electrochem. Soc.*, **141**, 2669 (1994).
9. P. Keller and H. Strehblow, "XPS investigations of Electrochemically Formed Passive Layers on Fe/Cr-alloys in 0.5 M H_2SO_4." *Corros. Sci.*, **46**, 1939 (2004).
10. K. Sugimoto and Y. Sawada, "The role of molybdenum additions to austenitic stainless steels tn the inhibition pitting in acid chloride solutions." *Corros. Sci.*, **17**, 425 (1977).
11. V. Maurice, H. Peng, L. H. Klein, A. Seyeux, S. Zanna, and P. Marcus, "Effects of molybdenum on the composition and nanoscale morphology of passivated austenitic stainless steel surfaces." *Faraday Discuss.*, **180**, 151 (2015).
12. E. De Vito and P. Marcus, "XPS study of passive films formed on molybdenum implanted austenitic stainless steels." *Surf. Interface Anal.*, **19**, 403 (1992).
13. I. Olefjord and B.-O. Elfstrom, "The composition of the surface during passivation of stainless steels." *Corrosion*, **38**, 46 (1982).
14. V. Maurice, W. P. Yang, and P. Marcus, "X-ray photoelectron spectroscopy and scanning tunneling microscopy study of passive films formed on (100) Fe-18Cr-13Ni single-crystal surfaces." *J. Electrochem. Soc.*, **145**, 909 (1998).
15. I. Olefjord, "The passive state of stainless steel." *Mater. Sci. Eng.*, **42**, 161 (1980).
16. H. Ogawa, H. Omata, I. Itoh, and H. Okada, "Auger electron spectroscopic and electrochemical analysis of the effect of alloying elelments on the passivation behaviour of stainless steels." *Corrosion*, **34**, 2 (1978).
17. I. Olefjord and L. Wegrelius, "Surface analysis of passive state." *Corros. Sci.*, **31**, 89 (1990).
18. Y. C. Lu, C. R. Clayton, and A. R. Brooks, "A bipolar model of the passivity of stainless steels—II. The influence of aqueous molybdate." *Corros. Sci.*, **29**, 863 (1989).
19. I. Olefjord, B. Brox, and U. Jelvestam, "Surface composition of stainless steels during anodic dissolution and passivation studied by ESCA." *J. Electrochem. Soc.*, **132**, 2854 (1985).
20. W. Yang, R.-C. Ni, H.-Z. Hua, and A. Pourbaix, "The behavior of chromium and molybdenum in the propagation process of localized corrosion of steels." *Corros. Sci.*, **24**, 691 (1984).
21. P. Street, "The nucleation and growth of passivation of corrosion pits on stainless steel." *Corros. Sci.*, **35**, 57 (1993).
22. Z. Wang, A. Seyeux, S. Zanna, and V. Maurice, "Chloride-induced alterations of the passive film on 316L stainless steel and blocking effect of pre-passivation." *Electrochim. Acta*, **329**, 135 (2020).
23. P. Street, "Aspects of the effects of electrolyte composition on the occurrence of metalstable pitting on stainless steel." *Corros. Sci.*, **36**, 525 (1994).
24. A. R. Brooks, C. R. Clayton, K. Doss, and Y. C. Lu, "On the Role of Cr in the passivity of stainless steel." *J. Electrochem. Soc.*, **133**, 2459 (1986).

25. M. Bojinov, G. Fabricius, T. Laitinen, K. Mäkelä, T. Saario, and G. Sundholm, "Influence of molybdenum on the conduction mechanism in passive films on iron–chromium alloys in sulphuric acid solution." *Electrochim. Acta*, **46**, 1339 (2001).
26. M. Tan, E. Akiyama, A. Kawashima, K. Asami, and K. Hashimoto, "The effect of air exposure on the corrosion behavior of amorphous Fe-8Cr-Mo-13P-7C alloys in 1 M HCl." *Corros. Sci.*, **37**, 1289 (1995).
27. L. Ma, F. Wiame, V. Maurice, and P. Marcus, "Origin of nanoscale heterogeneity in the surface oxide film protecting stainless steel against corrosion." *NPJ Mater. Degrad.*, **3**, 1 (2019).
28. L. Ma, F. Wiame, V. Maurice, and P. Marcus, "New insight on early oxidation stages of austenitic stainless steel from *in situ* XPS analysis on single-crystalline Fe-18Cr-13Ni." *Corros. Sci.*, **140**, 205 (2018).
29. L. Ma, F. Wiame, V. Maurice, and P. Marcus, "Stainless steel surface structure and initial oxidation at nanometric and atomic scales." *Appl. Surf. Sci.*, **494**, 8 (2019).
30. B. Lynch, S. Neupane, A. Seyeux, V. Maurice, and P. Marcus, "An XPS and ToF-SIMS study of the passive film formed on a model FeCrNiMo stainless steel surface in aqueous media after thermal pre-oxidation at ultra-low oxygen pressure." *App surf. science*, **554**, 149435 (2021).
31. B. Lynch, F. Wiame, Z. Wang, L. Ma, and E. Paschalidou,, "Passivation-induced Cr and Mo enrichments of 316L stainless steel surfaces and effects of controlled pre-oxidation." *J. Electrochem. Soc.*, **167**, 141509 (2020).
32. Z. Wang, E. M. Paschalidou, A. Seyeux, S. Zanna, V. Maurice, and P. Marcus, "Mechanisms of Cr and Mo enrichments in the passive oxide film on 316L austenitic stainless steel." *Front. Mater. Sci.*, **6**, 1 (2019).
33. L. Ma, E.-M. Paschalidou, F. Wiame, S. Zanna, V. Maurice, and P. Marcus, "Passivation mechanisms and pre-oxidation effects on model surfaces of FeCrNi austenitic stainless steel." *Corros. Sci.*, **167**, 108483 (2020).
34. B. Lynch, F. Wiame, V. Maurice, and P. Marcus, "XPS study of oxide nucleation and growth mechanisms on a model FeCrNiMo stainless steel surface." *App surf. science*, **575**, 151681 (2022).
35. L. Wang, A. Seyeux, and P. Marcus, "Ion transport mechanisms in the oxide film formed on 316L stainless steel surfaces studied by ToF-SIMS with $18O_2$ isotopic tracer." *J. Electrochem. Soc.*, **167**, 101511 (2020).
36. A. Elbiache and P. Marcus, "The role of molybdenum in the dissolution and the passivation of stainless steels with adsorbed sulfur." *Corros. Sci.*, **33**, 261 (1992).
37. G. O. Ilevbare and G. T. Burstein, "The role of alloyed molybdenum in the inhibition of pitting corrosion in stainless steels." *Corros. Sci.*, **43**, 485 (2001).
38. R. Qvarfortab, "Some observations regarding the influence of molybdenum on the pitting corrosion resistance of stainless steels." *Corros. Sci.*, **40**, 215 (1998).
39. Y. B. Lei, Z. B. Wang, B. Zhang, Z. P. Luo, J. Lu, and K. Lu, "Enhanced mechanical properties and corrosion resistance of 316L stainless steel by pre-forming a gradient nanostructured surface layer and annealing." *Acta Mater.*, **208**, 34 (2021).
40. M. Eifler, I. C. Garretson, B. S. Linke, J. Das, F. Torner, and J. Seewig, "Effects of vibratory finishing of 304 stainless steel samples on areal roughness parameters: a correlational analysis for anisotropy parameters." *J. Mater. Process. Technol.*, **273**, 1 (2019).
41. K. Rokosz, G. Solecki, G. Mori, R. Fluch, M. Kapp, and J. Lahtinen, "E ff ect of polishing on electrochemical behavior and passive layer composition of different stainless steels." *Materials*, **13**, 3402 (2020).
42. L. Ma, B. Lynch, F. Wiame, V. Maurice, and P. Marcus, "Nanoscale early oxidation mechanisms of model FeCrNi austenitic stainless steel surfaces at room temperature." *Corros. Sci.*, **190**, 109653 (2021).
43. S. B. Sharma, V. Maurice, L. H. Klein, and P. Marcus, "Local effects of organic inhibitor molecules on passivation of grain boundaries studied *In Situ* on copper." *J. Electrochem. Soc.*, **168**, 061501 (2021).
44. M. Bettayeb, V. Maurice, L. H. Klein, L. Lapeire, K. Verbeken, and P. Marcus, "Nanoscale intergranular corrosion and relation with grain boundary character as studied *In situ* on copper." *J. Electrochem. Soc.*, **165**, 1 (2018).
45. S. B. Sharma, V. Maurice, L. H. Klein, and P. Marcus, "*In situ* scanning tunneling microscopy study of 2-mercaptobenzimidazole local inhibition effects on copper corrosion at grain boundary surface terminations." *Electrochim. Acta*, **378**, 138150 (2021).
46. S. B. Sharma, V. Maurice, L. H. Klein, and P. Marcus, "Local Inhibition by 2-mercaptobenzothiazole of early stage intergranular corrosion of copper." *J. Electrochem. Soc.*, **167**, 161504 (2020).
47. M. Bettayeb, V. Maurice, L. H. Klein, L. Lapeire, K. Verbeken, and P. Marcus, "Combined *in situ* microstructural study of the relationships between local grain boundary structure and passivation on microcrystalline copper." *Electrochim. Acta*, **305**, 240 (2019).
48. Z. Wang, F. Di Franco, A. Seyeux, S. Zanna, V. Maurice, and P. Marcus, "Passivation-induced physicochemical alterations of the native surface oxide film on 316L austenitic stainless steel." *J. Electrochem. Soc.*, **166**, 11 (2019).
49. P. Klapetek, D. Necas, and C. Anderson, "Gwyddion user guide." *Version*, http://gwyddion.net/documentation/user-guide-en/ (2009).
50. S. Alignment, "The avantage data system." *Thermo Fisher Scientific*, N° 31005 (2008).
51. Z. Wang, C. Carrière, A. Seyeux, S. Zanna, D. Mercier, and P. Marcus, "XPS and ToF-SIMS investigation of native oxides and passive films formed on nickel alloys containing chromium and molybdenum." *J. Electrochem. Soc.*, **168**, 041503 (2021).
52. E. Gardin, S. Zanna, A. Seyeux, A. Allion-Maurer, and P. Marcus, "Comparative study of the surface oxide films on lean duplex and corresponding single-phase stainless steels by XPS and ToF-SIMS." *Corros. Sci.*, **143**, 403 (2018).
53. C. R. Clayton and Y. C. Lu, "A bipolar model of the passivity of stainless steels-III. The mechanism of MoO_4^{2-} formation and incorporation." *Corros. Sci.*, **29**, 881 (1989).
54. M. C. Biesinger, B. P. Payne, A. P. Grosvenor, L. W. M. Lau, A. R. Gerson, and R. S. C. Smart, "Resolving surface chemical states in XPS analysis of first row transition metals, oxides and hydroxides: Cr,Mn, Fe, Co and Ni." *Appl. Surf. Sci.*, **257**, 2717 (2011).
55. Z. Wang, D. Kong, M. Wang, G. Wang, and N. Li, "Sealing effect of surface porosity of Ti–P composite films on tinplates." *RSC Adv.*, **9**, 12990 (2019).
56. G. T. Burstein, P. C. Pistorius, and S. P. Mattin, "The nucleation and growth of corrosion pits on stainless steel." *Corros. Sci.*, **35**, 47 (1993).
57. G. S. Frankel, "Pitting corrosion of metals: a review of the critical factors." *J. Electrochem. Soc.*, **145**, 2186 (1998).
58. T. Massoud, V. Maurice, L. H. Klein, A. Seyeux, and P. Marcus, "Nanostructure and local properties of oxide layers grown on stainless steel in simulated pressurized water reactor environment." *Corros. Sci.*, **84**, 198 (2014).
59. M. Aronniemi, J. Sainio, and J. Lahtinen, "Chemical state quantification of iron and chromium oxides using XPS: the effect of the background subtraction method." *Surf. Sci.*, **578**, 108 (2005).